Multi-section matched-peak tomographic inversion with a moving source

E. K. Skarsoulis

Institute of Applied and Computational Mathematics, Foundation for Research and Technology Hellas,
P.O. Box 1527, 711 10 Heraklion, Crete, Greece

An extended matched-peak inversion approach is proposed for the simultaneous analysis of travel-time data from multiple tomographic sections, from a moving source to a number of peripheral fixed receivers, to estimate the position of the source and the ocean state along the various sections. The proposed solution consists of finding those model states and source positions that maximize the joint number of peak identifications in the arrival patterns measured simultaneously along all sections. The offset calibration problem, associated with the uncertainty regarding mooring positions and possible unresolved internal instrument delays, is also addressed using the peak-matching principle. The time offsets are estimated such that the total number of identifications, over all sections and all transmissions, is maximized. The same analysis also applies to the case of a moving receiver listening to a number of fixed sources. The proposed approach is applied for the analysis of 9-month-long travel-time data from four conodal sections of the Thetis-2 tomography experiment. © *2001 Acoustical Society of America.*
[DOI: 10.1121/1.1387092]

I. INTRODUCTION

Ocean acoustic travel-time tomography was introduced by Munk and Wunsch[1,2] as a remote-sensing technique for monitoring the ocean interior. Measuring the travel times of pulsed acoustic signals propagating through the water mass over a multitude of different paths, and exploiting the knowledge about how travel times are affected by the sound-speed (temperature) distribution in the water, the latter can be obtained by inversion. Nevertheless, the identification problem has to be solved first, i.e., the model arrival times must be associated with the observed travel times at the receiver.[3,4] Traditionally, this problem is solved by obtaining observed peak tracks (tracking problem) which are then associated with model peaks (identification problem), either manually or automatically.[5–9]

Recently, a matched-peak inversion approach was introduced[10] which by-passes the explicit solution of the tracking and identification problem. Using the linearized model relations between sound-speed and arrival-time perturbations about a set of background states, arrival times and associated model errors are calculated on a fine grid of model states discretizing the parameter space. Each model state can explain (identify) a number of observed peaks in a particular measurement lying within the uncertainty intervals of the corresponding predicted arrival times. The model states that explain the maximum number of observed peaks are considered as the more likely parametric descriptions of the measurement; these model states can be described in terms of mean values and variances providing a statistical answer (matched-peak solution) to the inversion problem. This approach has already been applied for the analysis (slice inversions) of large-scale tomography experiments, such as the 9-month-long Thetis-2 experiment in the western Mediterra-

nean sea[10,11] and the ongoing multi-year experiment in the Labrador sea.[12]

In the Thetis-2 experiment one of the moored transceivers failed to receive tomography signals from other instruments as well as navigation signals from its associated bottom transponders used for motion tracking. The particular transceiver acted only as a source during the 9 months of the experiment. Its signals were recorded at a number of receivers within the tomographic array; nevertheless, the corresponding arrival times could not be corrected for the motion of the source, due to lack of navigation data, and thus absolute-time inversions could not be performed. In the present work the matched-peak approach is extended to allow the simultaneous analysis of travel-time data from multiple tomographic sections, from a moving source to a number of peripheral fixed receivers, to estimate the position of the source and the ocean state along the various sections. The proposed approach exploits the estimated peak arrival times from the simultaneous acoustic transmissions along the sections. The solution consists of finding the population of model states and source positions that maximize the joint number of peak identifications, over all sections. The same analysis also applies to the case of a moving receiver listening to a number of fixed sources.

Cornuelle[13] introduced a unified probabilistic approach for solving the inversion, mooring-motion, and clock-drift estimation problem for an arbitrary number of moving transceivers using ray theory and linear model relations (between ocean parameters and travel times). Gaillard[14] adapted a deterministic ray inversion scheme, introduced by Munk and Wunsch,[15] to the case of moving transceivers, assuming ocean perturbations about a canonical sound-speed profile. Also in that work the case was treated where three sources at fixed locations are used to track a moving receiver in the middle, simultaneously with the inversions along the three

sections. These approaches are simple and generic. Nevertheless, they both assume that identified peak tracks exist, and they also rely on linear model relations. The matched-peak approach applies directly to the estimated travel times, without requiring the identification problem to be solved beforehand, thus enabling the automatic analysis of travel-time data; furthermore, considering the background state as an unknown, the case of nonlinear model relations can be treated.

The lack of knowledge of the exact mooring positions, i.e., of the exact horizontal distance between any two moorings, and possible unresolved internal instrument delays cause a travel-time offset. This offset is usually estimated (and removed) by comparing acoustic measurements with acoustic predictions based on existing hydrographic measurements; this requires simultaneous acoustic and hydrographic measurements along each section.[9] In the case of multiple conodal sections a calibration method is proposed here, which is based on the peak-matching principle and which maximizes the total number of identifications over all sections and all transmissions. This calibration approach is based on acoustic data only, i.e., it does not require additional hydrographic measurements.

The contents of the work are organized as follows: Section II addresses the model relations between acoustic travel times and ocean parameters, as well as further sources of travel-time variability, such as mooring motion, clock drift, and time offsets. The derivative of arrival times with respect to the source–receiver range is expressed analytically using the notion of peak arrivals and normal-mode theory. In Sec. III the inversion problem for the case of multiple sections with a central moving transceiver is addressed, using the matched-peak approach. In the case of small transceiver displacements an invariance property of the matched-peak estimates of the time offsets is proven and discussed. In Sec. IV the proposed method is used for the analysis of 9-month-long travel-time data from four conodal sections of the Thetis-2 tomography experiment conducted from January to October 1994 in the western Mediterranean Sea. Further, a synthetic test case, based on the Thetis-2 data with simulated transceiver displacements, is considered. In Sec. V the main features of the proposed approach are discussed and conclusions are drawn.

II. MODEL RELATIONS AND TRAVEL-TIME VARIABILITY

A tomographic setting is considered with a broadband source and a distant receiver in a range-independent ocean. Due to the multi-path nature of acoustic propagation, a pulsed signal emitted by the source will arrive at the receiver as a sequence of peaks (the acoustic arrivals) at different time instants. The arrival times of the peaks can be modeled as functionals of the sound-speed profile $c(z)$ by expressing the arrival pattern a, defined as the amplitude of the acoustic pressure p_r at the receiver in the time domain, through the inverse Fourier transform

$$a(t;c;R,z_s,z_r) = |p_r(t;c;R,z_s,z_r)|$$

$$= \frac{1}{2\pi} \left| \int_{-\infty}^{\infty} H_{sr}(\omega;c;R,z_s,z_r) P_s(\omega) e^{j\omega t} \, d\omega \right|, \quad (1)$$

where $P_s(\omega)$ is the source signal in the frequency domain and $H_{sr}(\omega;c;R,z_s,z_r)$ is the Green's function. The latter depends on the circular frequency ω, the sound-speed profile $c(z)$, and the relative source/receiver locations, i.e., on the source–receiver range R, the source and receiver depth z_s and z_r, respectively. From the mathematical viewpoint the arrivals can be defined as the local maxima of the arrival pattern with respect to time[16]

$$\frac{\partial a}{\partial t}(\tau_i;c;R,z_s,z_r) = 0, \quad i = 1,\ldots,I. \quad (2)$$

This definition of arrivals (peak arrivals) is generic and encompasses the notions of ray arrivals[1,17] and modal arrivals[18,19] as special cases; it can also cope with any modeling approach for the arrival pattern, either ray- or wave theoretic. Since the arrival pattern depends on the sound-speed profile and the source–receiver locations, the peak arrival times do so as well, i.e., $\tau_i = \tau_i(c;R,z_s,z_r)$.

The sound-speed variability in a certain area can be represented through a modal expansion

$$c(z) = c_0(z) + \sum_{l=1}^{L} \vartheta_l f_l(z), \quad (3)$$

where $c_0(z)$ is a basic reference profile and $f_l(z)$, $l = 1,\ldots,L$, is a set of sound-speed modes, e.g., empirical orthogonal functions (EOFs).[20] The functional dependence of τ_i on the sound speed, assuming fixed source/receiver positions, can be written as a parametric dependence on the modal parameter vector $\boldsymbol{\vartheta} = (\vartheta_1,\ldots,\vartheta_L)'$

$$\tau_i = g_i(\boldsymbol{\vartheta}), \quad i = 1,2,\ldots,I, \quad \boldsymbol{\vartheta} \in \Theta, \quad (4)$$

where Θ is the parameter domain spanning the anticipated sound-speed variability. Although the dependence $g_i(\boldsymbol{\vartheta})$ is in general nonlinear, in the case of small variations about a background state $\boldsymbol{\vartheta}^{(b)}$ it can be linearized

$$\boldsymbol{\tau}(\boldsymbol{\vartheta}) = \boldsymbol{\tau}^{(b)} + \mathbf{G}^{(b)}(\boldsymbol{\vartheta} - \boldsymbol{\vartheta}^{(b)}), \quad (5)$$

where $\boldsymbol{\tau} = (\tau_1,\ldots,\tau_I)'$ is the arrival-time vector, $\boldsymbol{\tau}^{(b)} = \boldsymbol{\tau}(\boldsymbol{\vartheta}^{(b)})$ denotes the background arrival times, and $\mathbf{G}^{(b)}$ is the observation (influence) matrix corresponding to the background state $\boldsymbol{\vartheta}^{(b)}$ and relating the sound-speed and travel-time variability, $G_{il}^{(b)} = \partial g_i(\boldsymbol{\vartheta}^{(b)})/\partial \vartheta_l$. Using the notions of ray, modal, or peak arrivals, the matrix $\mathbf{G}^{(b)}$ can be analytically expressed in terms of background quantities,[16,17,21] and Eq. (5) can be used as a basis for linear $\boldsymbol{\vartheta}$ inversions of travel-time data.

In the case where the nonlinear dependence of the arrival times on the sound-speed parameters becomes significant (e.g., large sound-speed variations), the above linearization about a single background state is insufficient and cannot be used for inversions. Nevertheless, it can be extended in a straightforward manner by considering a set of discrete background states, rather than a single background

state, whose extent depends on the anticipated sound-speed variability and the degree of nonlinearity;[9] then, Eq. (5) can be used with respect to the nearest background state each time. In this connection, the index b will be considered in the following as a variable, $b \in \mathcal{B}$, from the set $\mathcal{B}$ of discrete background states. Thus, the nonlinear model relation (4) is replaced by a set of linear ones. The cost to be paid, with respect to the inverse problem, is that an additional unknown is introduced, the background variable b.

In addition to sound-speed changes there are also other sources of travel-time variability in a range-independent ocean environment, such as mooring motions and clock drifts. Furthermore, the lack of knowledge of the exact mooring positions, and possible unresolved internal instrument delays cause travel-time offsets and displacements that have to be accounted for. Taking these factors into account, the observed travel times $\boldsymbol{\tau}^{(o)}$ can be written in the form

$$\boldsymbol{\tau}^{(o)} = \boldsymbol{\tau}^{(b)} + \mathbf{G}^{(b)}(\boldsymbol{\vartheta} - \boldsymbol{\vartheta}^{(b)}) + \frac{\partial \boldsymbol{\tau}}{\partial R}(\delta r + \Delta R)$$
$$+ \mathbf{u}(\delta t + \Delta T) + \boldsymbol{\nu}. \tag{6}$$

The vector $\partial \boldsymbol{\tau}/\partial R$ is the derivative of travel times with respect to the horizontal source–receiver range. The variable δr denotes the range perturbation due to mooring motion, whereas ΔR denotes the difference of the actual distance between moorings (after deployment) and the assumed (best estimated) distance used for acoustic modeling. The vertical motions of the source or receiver are not accounted for here. One reason is that for moored instruments and small mooring deviations from the vertical, displacements in the vertical are much smaller than in the horizontal. Furthermore, the derivative of travel times with respect to the vertical mooring displacement for typical underwater propagation conditions has been estimated by Cornuelle[13] to be about one order of magnitude smaller than the horizontal-motion derivative.[22]

If the source and receiver location is tracked during the experiment, e.g., through bottom-mounted navigation transponders, the range perturbation δr can be estimated for each transmission and the corresponding mooring motion effect can be removed from the observed travel times. Since the source and the receiver change their positions with time, following the mooring motions, the range perturbation δr will be in general different from transmission to transmission. The deviation ΔR, on the other hand, is a constant which accounts for the difference between the actual and the nominal (best estimated) source–receiver range, which remains even after removal of the mooring-motion effect. Since the mooring locations can be known today with GPS accuracy, the correction ΔR will be of the order of a few meters at most.

The vector $\mathbf{u}$ in (6) is a unity vector, with all its elements equal to 1. The variable δt denotes the differential clock drift, i.e., the difference between receiver and source clock drifts, during the experiment. This is expected to be a smooth function of time and is commonly approximated by a low-order polynomial. The term ΔT accounts for a differential internal instrument delay which is assumed constant. Finally,

the vector $\boldsymbol{\nu}$ in (6) accounts for the cumulative modeling and observation error.

A. Range derivatives of arrival times

As already mentioned, the arrival pattern a—and thus the arrival times—in a range-independent ocean environment depend on the sound-speed profile and also on the location of the source and receiver, i.e., on the source–receiver range and depths. Applying Eq. (2) at a perturbed range and using a Taylor expansion about the unperturbed state, the following expression can be obtained for the derivative of peak arrival times with respect to the source–receiver range:

$$\frac{\partial \tau_i}{\partial R} = \frac{-\dfrac{\partial^2 a(\tau_i; c; R, z_s, z_r)}{\partial R \partial t}}{\dfrac{\partial^2 a(\tau_i; c; R, z_s, z_r)}{\partial t^2}}. \tag{7}$$

The time derivatives of the arrival pattern can be obtained from H_{sr} through (1) by using elementary properties of the Fourier transform. Further, the calculation of $\partial a/\partial R$ can be reduced to the calculation of H_{sr} and $\partial H_{sr}/\partial R$.[16] The expression (7) is generic and can be used in connection with any propagation model, either geometric or wave theoretic. Using normal-mode theory[23,24] the Green's function H_{sr} in the far field can be written as a sum of modes

$$H_{sr}(\omega; c; R, z_s, z_r) = \frac{\omega \rho^2}{\sqrt{8\pi}} \sum_{n=1}^{N} \frac{u_n(z_s) u_n(z_r)}{\sqrt{k_n R}}$$
$$\times \exp\{j k_n R - j\pi/4\}, \tag{8}$$

where ρ is the water density. The quantities k_n and u_n, $n = 1, ..., N$ are the real eigenvalues and the corresponding eigenfunctions (propagating modes), respectively, of the vertical Sturm–Liouville problem

$$\frac{d^2 u_n(z)}{dz^2} + \frac{\omega^2}{c^2(z)} u_n(z) = k_n^2 u_n(z), \tag{9}$$

supplemented by the conditions that $u_n = 0$ at the sea surface, ρu_n and du_n/dz are continuous across the interfaces, and u_n and du_n/dz are vanishing as $z \to \infty$. The range derivative of the Green's function (8) can be expressed as

$$\frac{\partial H_{sr}}{\partial R} = -\frac{1}{2R} H_{sr} + \frac{\omega \rho^2}{\sqrt{8\pi}} \sum_{n=1}^{N} k_n \frac{u_n(z_s) u_n(z_r)}{\sqrt{k_n R}}$$
$$\times \exp\{j k_n R + j\pi/4\}. \tag{10}$$

The first term in the above expression is due to the variation of the geometrical attenuation term $\sqrt{k_n R}$. The second term is due to the phase variation and is dominant, since the first term contains the range R in the denominator. Using the above expressions (8) and (10), in connection with (1) and (7), the range derivatives of the peak arrival times can be calculated.

Table I shows calculated values of these derivatives for eight peak arrivals along four Thetis-2 sections (details are given in Sec. IV). It is seen from this table that early arrivals are characterized by smaller values of the range derivatives than late arrivals. Furthermore, the range of values is very

TABLE I. Range derivatives of peak-arrival times based on normal-mode calculations for four Thetis-2 sections.

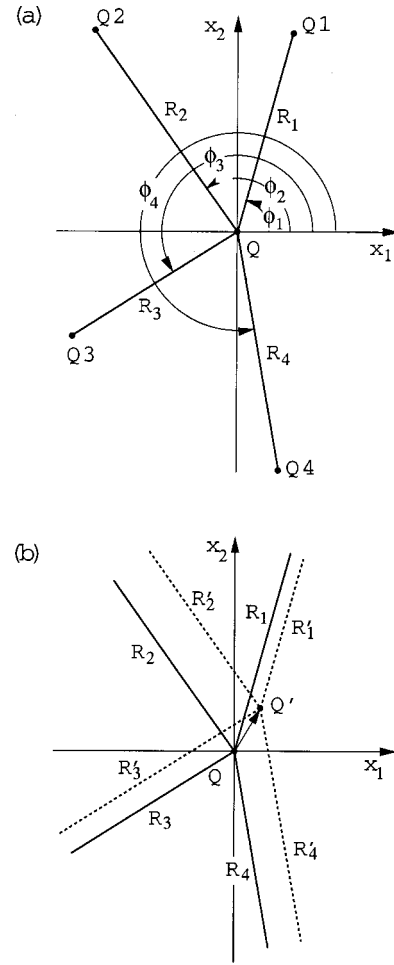| τ_i (s)	$\partial \tau_i / \partial R$ (s/m)	τ_i (s)	$\partial \tau_i / \partial R$ (s/m)
H-W4		W5-W4	
201.474	$6.626 \cdot 10^{-4}$	157.361	$6.617 \cdot 10^{-4}$
201.053	$6.612 \cdot 10^{-4}$	157.161	$6.602 \cdot 10^{-4}$
200.995	$6.607 \cdot 10^{-4}$	157.078	$6.592 \cdot 10^{-4}$
200.924	$6.587 \cdot 10^{-4}$	157.024	$6.586 \cdot 10^{-4}$
200.841	$6.576 \cdot 10^{-4}$	156.963	$6.566 \cdot 10^{-4}$
200.697	$6.552 \cdot 10^{-4}$	156.851	$6.554 \cdot 10^{-4}$
200.494	$6.534 \cdot 10^{-4}$	156.665	$6.527 \cdot 10^{-4}$
200.186	$6.497 \cdot 10^{-4}$	156.343	$6.483 \cdot 10^{-4}$
S-W4		W3-W4	
169.404	$6.646 \cdot 10^{-4}$	235.091	$6.632 \cdot 10^{-4}$
169.218	$6.616 \cdot 10^{-4}$	234.864	$6.604 \cdot 10^{-4}$
169.123	$6.591 \cdot 10^{-4}$	234.717	$6.587 \cdot 10^{-4}$
169.052	$6.578 \cdot 10^{-4}$	234.632	$6.576 \cdot 10^{-4}$
168.947	$6.563 \cdot 10^{-4}$	234.534	$6.568 \cdot 10^{-4}$
168.793	$6.546 \cdot 10^{-4}$	234.375	$6.541 \cdot 10^{-4}$
168.544	$6.509 \cdot 10^{-4}$	234.136	$6.520 \cdot 10^{-4}$
168.124	$6.462 \cdot 10^{-4}$	233.789	$6.485 \cdot 10^{-4}$

FIG. 1. (a) The geometry of multiple conodal sections defined by a central transceiver Q and a set of peripheral transceivers Q1, Q2, etc. (b) Perturbed geometry due to a horizontal displacement of the central transceiver (detail).

small, from above $6.45 \cdot 10^{-4}$ s/m to less than $6.65 \cdot 10^{-4}$ s/m for all sections; the variability in all cases is less than 3%. Thus, a 10-m range increase will cause a time delay of about 6.45 ms to the earliest arrivals and 6.65 ms to the latest ones; i.e., the relative displacement of the arrivals will be as small as 0.2 ms. On the other hand, a 1000-m range increase will cause a delay of about 645 ms to the early arrivals and 665 ms to the late ones; i.e., the arrival pattern will stretch by approximately 20 ms. These findings are in agreement with the results by Cornuelle[13] for the range derivatives of ray-arrival times

$$\frac{\partial \tau_i}{\partial R} = \frac{\cos \psi_{r,i}}{c(z_r)} = \frac{\cos \psi_{s,i}}{c(z_s)}, \tag{11}$$

where $\psi_{r,i}$ and $\psi_{s,i}$ are the grazing angle of the ith eigenray at the source and at the receiver, respectively. Since ray grazing angles are typically less than 12 deg, with larger angles corresponding to earlier ray arrivals, using a typical sound speed of 1500 m/s yields a range for the derivative values similar to that obtained for the peak arrivals above.

In conclusion, a range variation causes a translation and a relative deformation (stretching/shrinking) to the arrival pattern. The translation effect is dominant while the deformation is much weaker. If the range variation is small, of the order of a few tens of meters, the deformation effect is very small, of the order of 1 ms. As mentioned earlier, the magnitude ΔR, accounting for the difference between actual and nominal (best estimated from GPS) mooring distance, is expected to reach a few meters at most. In this connection, the stretching/shrinking effect of ΔR on the travel times can be neglected. Since the remaining translation effect due to ΔR is similar to the effect of the internal instrument delay ΔT, the two effects can be merged in (6), resulting in

$$\boldsymbol{\tau}^{(o)} = \boldsymbol{\tau}^{(b)} + \mathbf{G}^{(b)} (\boldsymbol{\vartheta} - \boldsymbol{\vartheta}^{(b)}) + \frac{\partial \boldsymbol{\tau}}{\partial R} \delta r + \mathbf{u}(\delta t + \Delta T) + \boldsymbol{\nu}. \tag{12}$$

III. MULTI-SECTION MATCHED-PEAK INVERSION

In this section the matched-peak approach is applied to travel-time data from multiple conodal tomographic sections, e.g., from a moving source to a number of peripheral fixed receivers, as shown in Fig. 1(a). The same analysis also applies to the case of a moving receiver listening to a number of fixed sources. The observed travel-time data in the simultaneous transmissions along the various sections will be exploited in order to estimate the position of the central transceiver, the ocean state, and the constant offset along each section. Clock-drift errors are not accounted for, i.e., it is assumed that the observed arrival times have been corrected for the differential clock drift.

Any deviation of the central mooring from the vertical will induce a horizontal displacement $\mathbf{x} = (x_1, x_2)$ to the central transceiver which in turn will affect the horizontal range of each section. Assuming that the horizontal deviations of the central transceiver are much smaller than the horizontal ranges of the sections, the perturbed sections will be nearly parallel to the nominal ones, as shown in Fig. 1(b), and thus the change in range for each section will be given by the projection of the vector $\mathbf{x}$ on the original section direction

$$\delta r_s(\mathbf{x}) = -x_1 \cos \phi_s - x_2 \sin \phi_s, \quad s = 1, \ldots, S, \tag{13}$$

where ϕ_s is the angle that section s builds with the axis x_1, as shown in Fig. 1(a), and δr_s the range perturbation of section s due to $\mathbf{x}$. The subscript s is used in the following to denote section-specific quantities. Neglecting the clock-drift term from (12), the observed travel times for the sth section become

$$\boldsymbol{\tau}_s^{(o)} = \boldsymbol{\tau}_s^{(b)} + \mathbf{G}_s^{(b)}(\boldsymbol{\vartheta}_s - \boldsymbol{\vartheta}_s^{(b)}) + \frac{\partial \boldsymbol{\tau}_s}{\partial R_s} \delta r_s(\mathbf{x}) + \mathbf{u}_s \Delta T_s + \boldsymbol{\nu}_s .$$
(14)

For each set of simultaneous transmissions the unknowns are the horizontal displacement $\mathbf{x}$ of the central transceiver, the background state b_s, and the parameter vector $\boldsymbol{\vartheta}_s$ (or, alternatively, the perturbation $\boldsymbol{\vartheta}_s - \boldsymbol{\vartheta}_s^{(b)}$), $s = 1,...,S$, along each section. In addition, the constants (offsets) ΔT_s have to be estimated.

In the matched-peak approach the parameter domain referring to each section is discretized into a regular grid, with discretization steps $\delta \boldsymbol{\vartheta}_s$,[10] which is superposed on the grid of background states for that section. Using the model relations, arrival-time predictions are made for each discrete model state $\widetilde{\boldsymbol{\vartheta}}_s$ (a tilde denotes quantities referring to the discretization grid), depending also on the displacement $\mathbf{x}$ and the constant ΔT_s

$$\widetilde{\boldsymbol{\tau}}_s(\widetilde{\boldsymbol{\vartheta}}_s;\mathbf{x};\Delta T_s) = \boldsymbol{\tau}_s^{(b)} + \mathbf{G}_s^{(b)}(\widetilde{\boldsymbol{\vartheta}}_s - \boldsymbol{\vartheta}_s^{(b)}) + \frac{\partial \boldsymbol{\tau}_s}{\partial R_s} \delta r_s(\mathbf{x})$$
$$+ \mathbf{u}_s \Delta T_s .$$
(15)

Each discrete model state corresponds to a particular background state. An estimate for the upper bound of the prediction error is given by the sum of the observation/modeling error $\boldsymbol{\nu}_s$ and a discretization error, which depends on the background state and the discretization steps

$$\mathbf{e}_s(b_s, \delta \boldsymbol{\vartheta}_s) = \tfrac{1}{2}|\mathbf{G}_s^{(b)}| \delta \boldsymbol{\vartheta}_s + \boldsymbol{\nu}_s ,$$
(16)

where $|\mathbf{G}_s^{(b)}|$ denotes the matrix whose elements are the absolute values of the elements of $\mathbf{G}_s^{(b)}$. Each of the predicted arrival times (15) is allowed to associate with observed arrival times if its time difference is smaller than the corresponding travel-time error (16). A matching index Λ_s can be thus calculated along each section, depending on $\widetilde{\boldsymbol{\vartheta}}_s$, $\mathbf{x}$, and ΔT_s, and denoting the number of identifiable peaks, i.e., the number of peaks in the measured arrival pattern that can be associated with the predicted arrival times $\widetilde{\boldsymbol{\tau}}_s(\widetilde{\boldsymbol{\vartheta}}_s;\mathbf{x};\Delta T_s)$

$$\Lambda_s = \Lambda_s(\widetilde{\boldsymbol{\vartheta}}_s;\mathbf{x};\Delta T_s).$$
(17)

Λ_s can be calculated in a straightforward and simple way as explained in Ref. 10; the associated computational burden is much smaller than for building up the set of all possible trial identifications (possible associations between predicted and observed peaks), which is necessary, e.g., for explicitly solving the identification problem.[9]

According to the peak-matching principle, the sound-speed parameters $\boldsymbol{\vartheta}_s$ along the various sections and the horizontal displacement $\mathbf{x}$ of the central transceiver can be estimated from each set of simultaneous transmissions, for given offsets ΔT_s, by finding the population of discrete model states and corresponding displacements that maximize the joint number of peak identifications over all sections

$$V(\Delta \mathbf{T}) = \left\{ (\widetilde{\boldsymbol{\vartheta}}_1,...,\widetilde{\boldsymbol{\vartheta}}_S;\mathbf{x}) : \sum_{s=1}^{S} \Lambda_s(\widetilde{\boldsymbol{\vartheta}}_s;\mathbf{x};\Delta T_s) = \max \right\}, \quad (18)$$

where $\Delta \mathbf{T} = (\Delta T_1,...,\Delta T_S)$ denotes the vector of offsets along all sections. The maximum value of the joint matching index corresponding to the elements of $V(\Delta \mathbf{T})$ is denoted by $M(\Delta \mathbf{T})$

$$(\widetilde{\boldsymbol{\vartheta}}_1,...,\widetilde{\boldsymbol{\vartheta}}_S;\mathbf{x}) \in V(\Delta \mathbf{T}) \Leftrightarrow \sum_{s=1}^{S} \Lambda_s(\widetilde{\boldsymbol{\vartheta}}_s;\mathbf{x};\Delta T_s)$$
$$= M(\Delta \mathbf{T}).$$
(19)

Since $\Delta \mathbf{T}$ is valid for the entire experiment duration, from deployment to recovery, it is estimated from the entire data set, i.e., from the entirety of the sets of simultaneous transmissions. Assuming that there are K sets of simultaneous transmissions along the sections considered, and denoting by $M_k(\Delta \mathbf{T})$ the maximum of the joint matching index corresponding to the kth transmission set, the matched-peak estimate of $\Delta \mathbf{T}$ is set to maximize the sum $\mathcal{M}(\Delta \mathbf{T}) = \Sigma_{k=1}^{K} M_k(\Delta \mathbf{T})$ over all transmissions. It is shown in the following subsection, for the case of small motions, that this estimate is not a unique one, but rather a class

$$\mathcal{D} = \{ \Delta \mathbf{T} : \mathcal{M}(\Delta \mathbf{T}) = \max \}$$
(20)

of estimates, based on the fact that the global matching index $\mathcal{M}$ is invariant to translations of the (x_1,x_2) coordinate system. The maximum of the global matching index, over all sections and all transmissions, corresponding to the elements of $\mathcal{D}$, will be denoted by $\mathcal{M}_{\max}$

$$\Delta \mathbf{T} \in \mathcal{D} \Leftrightarrow \mathcal{M}(\Delta \mathbf{T}) = \mathcal{M}_{\max} .$$
(21)

In summary, the offset calibration (determination of $\Delta \mathbf{T}$) is performed by maximizing the global matching index, over all sections and all transmissions. At the level of each single set of simultaneous transmissions the oceanographic inversion problem along the sections as well as the navigation problem for the central transceiver is solved by maximizing the joint matching index, over all sections. In other words, using probabilistic terminology, the offset calibration problem is solved by maximizing the marginal likelihood over all sections and transmissions, the likelihood being represented by the matching index for each section and each transmission, whereas the oceanographic inversion and navigation problems are solved at the level of each single set of simultaneous transmissions, by maximizing the marginal likelihood over all sections.

A. Small motions

If the horizontal displacement $\mathbf{x}$ of the central transceiver is small, the range effects on the arrival pattern can be considered limited to the translation only, since the time stretching/shrinking of the arrival pattern will be negligible, as discussed in Sec. II A. In the matched-peak context, negligible means that it is small compared to the cumulative observation, modeling, and discretization errors. For assumed errors of the order of 10 ms, horizontal displacements

up to about 50 m can be considered to be small, since the induced relative deformation of the arrival pattern is less than 1 ms. The horizontal displacements of the Thetis-2 transceivers are of the above order and can thus be considered as small motions. Neglecting the deformation effect of the horizontal displacement $\mathbf{x}$, the arrival-time predictions are written in the form

$$\widetilde{\boldsymbol{\tau}}_s(\widetilde{\boldsymbol{\vartheta}}_s;\mathbf{x};\Delta T_s) = \boldsymbol{\tau}_s^{(b)} + \mathbf{G}_s^{(b)}(\widetilde{\boldsymbol{\vartheta}}_s - \boldsymbol{\vartheta}_s^{(b)})$$
$$+ \mathbf{u}_s(c_r^{-1}\delta r_s(\mathbf{x}) + \Delta T_s), \qquad (22)$$

where c_r is an arbitrary reference sound speed, e.g., 1500 m/s (a change in c_r of 10 m/s will cause a travel-time error as small as 0.2 ms).

It is shown in the following that if $\Delta \mathbf{T}$ belongs to $\mathcal{D}$, then any other delay vector $\Delta \mathbf{T}'$ defined through the relation

$$\Delta T_s' = \Delta T_s + A_1 \cos \phi_s + A_2 \sin \phi_s, \quad s = 1,2,...,S, \quad (23)$$

where A_1 and A_2 are constants, will also belong to $\mathcal{D}$. Substituting (23) into (22) and taking into account the kinematic condition (13), the predicted arrival times can be written

$$\widetilde{\boldsymbol{\tau}}_s(\widetilde{\boldsymbol{\vartheta}}_s;\mathbf{x};\Delta T_s) = \boldsymbol{\tau}_s^{(b)} + \mathbf{G}_s^{(b)}(\widetilde{\boldsymbol{\vartheta}}_s - \boldsymbol{\vartheta}_s^{(b)})$$
$$+ \mathbf{u}_s(c_r^{-1}\delta r_s(\mathbf{x} + c_r\mathbf{A}) + \Delta T_s')$$
$$= \widetilde{\boldsymbol{\tau}}_s(\widetilde{\boldsymbol{\vartheta}}_s;\mathbf{x} + c_r\mathbf{A};\Delta T_s'), \qquad (24)$$

where $\mathbf{A} = (A_1, A_2)$. The above equality of the predicted arrival times for $\Delta \mathbf{T}$ and $\Delta \mathbf{T}'$, for the same discrete model state $\widetilde{\boldsymbol{\vartheta}}_s$ but different displacements $\mathbf{x}$ and $\mathbf{x} + c_r\mathbf{A}$, respectively, passes to the matching index for each section at the level of a single transmission

$$\Lambda_s(\widetilde{\boldsymbol{\vartheta}}_s;\mathbf{x};\Delta T_s) = \Lambda_s(\widetilde{\boldsymbol{\vartheta}}_s;\mathbf{x} + c_r\mathbf{A};\Delta T_s'), \qquad (25)$$

which in turn results in identical optimum (maximum) values for the joint matching indices

$$M(\Delta \mathbf{T}) = M(\Delta \mathbf{T}'). \qquad (26)$$

In the case of K sets of simultaneous transmissions, Eq. (26) holds for each set of simultaneous transmissions, i.e., it becomes $M_k(\Delta \mathbf{T}) = M_k(\Delta \mathbf{T}')$, $k = 1,...,K$. The global matching index corresponding to $\Delta \mathbf{T}'$ will then read

$$\mathcal{M}(\Delta \mathbf{T}') = \sum_{k=1}^{K} M_k(\Delta \mathbf{T}') = \sum_{k=1}^{K} M_k(\Delta \mathbf{T})$$
$$= \mathcal{M}(\Delta \mathbf{T}) = \mathcal{M}_{\max}, \qquad (27)$$

since $\Delta \mathbf{T} \in \mathcal{D}$. Equation (27) implies that $\Delta \mathbf{T}'$ also belongs to $\mathcal{D}$. Accordingly, for each offset vector $\Delta \mathbf{T}$ in $\mathcal{D}$ there is a multiplicity of equivalent offset vectors $\Delta \mathbf{T}'$ which correspond to translations of the (x_1, x_2)-coordinate system; the transformation (23), in particular, corresponds to a translation by $c_r\mathbf{A}$. Consequently, any two components of $\Delta \mathbf{T}$ can be arbitrarily fixed, e.g., $\Delta T_1 = \Delta T_2 = 0$; i.e., the dimension of the $\Delta \mathbf{T}$ search can be reduced by 2. From the above it is clear that the global matching index $\mathcal{M}(\Delta \mathbf{T})$ and the associated model states at the level of each section and each transmission are invariant to translations of the (x_1, x_2)-coordinate system. The same can be shown to be
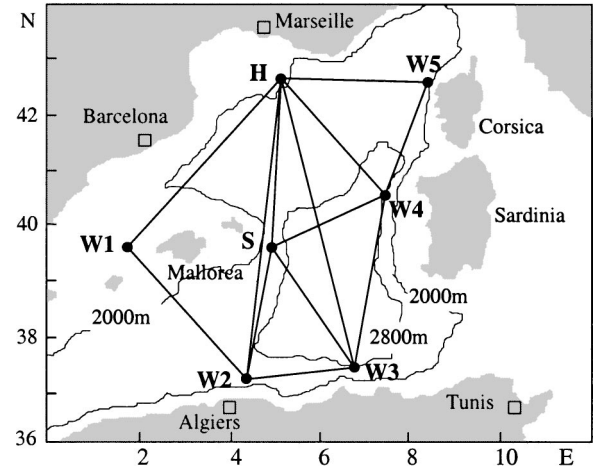

FIG. 2. The geometry of the Thetis-2 experiment in the western Mediterranean Sea.

also true for rotations, which however do not affect the dimensionality of the ΔT-search.

IV. APPLICATION TO THETIS-2 EXPERIMENT

In this section the proposed inversion approach is applied to multi-section travel-time data from the Thetis-2 tomography experiment conducted from January to October 1994 in the western Mediterranean Sea.[11,25] Figure 2 shows the experimental site and geometry. The tomographic array contained seven moored transceivers, all deployed at a nominal depth of 150 m. An HLF-5 source, marked by H, of central frequency 250 Hz and effective bandwidth 62.5 Hz, insonified the basin at 8-h intervals. The remaining six sources (W1–W5 and S), transmitting six times per day, were of Webb type with central frequency 400 Hz and effective bandwidth 100 Hz. The receiver parts of H and S could listen to 400-Hz signals only, whereas the receivers at W1–W5 were modified to listen to both 400-Hz and 250-Hz signals.

After completion of the experiment it was discovered that the instrument W4 had very few good records. A leakage had resulted in a short circuit at both the receiver and navigation inputs, such that neither navigation nor receiver data were available at this instrument.[26] Fortunately, the W4 transmitter continued to work properly and the W4 transmissions were recorded at the other instruments, in particular at W3, W5, H, and S. These receptions, however, cannot be corrected for the motions of W4 due to missing navigation data. Accordingly, absolute-time inversions cannot be performed along the corresponding sections. The multi-section matched-peak inversion method is applied in the following to the sections W3–W4, W5–W4, H–W4, and S–W4, with nominal ranges 354.7, 237.2, 303.5, and 255.4 km, respectively, to simultaneously estimate the ocean state and navigate the source W4.

A. Data

Figure 3 shows the observed peak arrival times (light dots) and cutoff peaks (heavier dots) corresponding to the daily averaged transmissions along the four sections, after

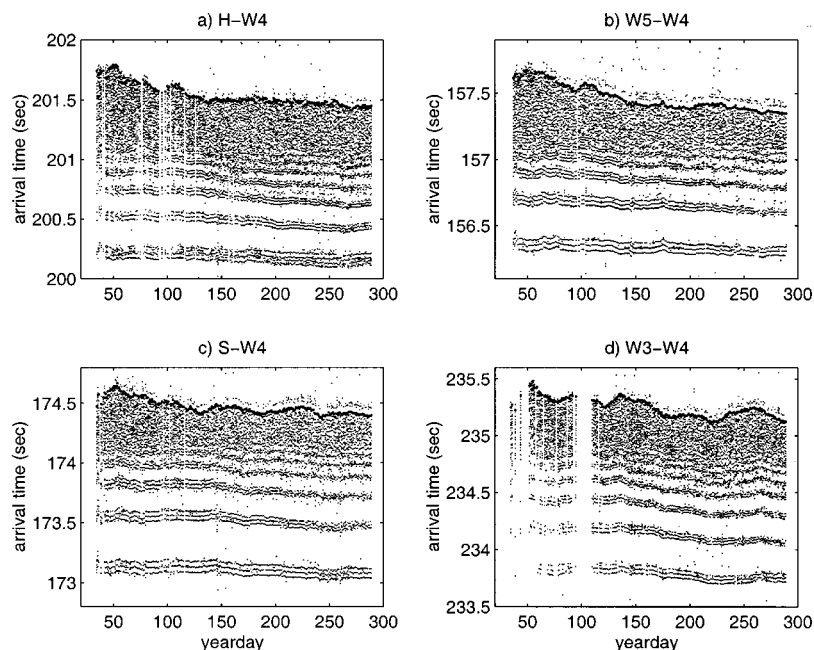E. K. Skarsoulis: Multi-section matched-peak inversion 791

FIG. 3. Measured arrival times from W4 at H, W5, S, and W3, respectively. The cutoff peaks are denoted by heavier dots.

correlation processing and clock-drift correction. Mooring-motion correction has also been applied for all instruments except W4, i.e., the data of Fig. 3 contain the cumulative effects of ocean changes and W4 motions. The horizontal axes in Fig. 3 represent yeardays of 1994 and span the 9-month duration of the experiment, whereas the vertical axes measure travel times. Low-SNR receptions have been omitted from this figure and are neglected in the subsequent analysis. It is seen, e.g., in Fig. 3(d) that there is a nearly 15-day interruption in the W3–W4 data, around yearday 100; during this period the simultaneous four-section inversion cannot be applied.

Five to six arrival groups can be distinguished in the early part of most receptions along the four sections. These can be associated with particular ray groups corresponding to steep propagation angles. The remaining intermediate and late arrivals are difficult to interpret in terms of ray arrivals because ray groups overlap with each other in this interval. To exploit some of the information contained in the intermediate and late part of the arrival patterns the peak-arrival approach[8,16] is used, combined with normal-mode propagation modeling.

Figure 4 shows the basic reference sound-speed profile for each section and also the three most significant EOFs for the western Mediterranean basin. The historical rms values of the EOF amplitudes are $\vartheta_{1,rms} = 18.48$, $\vartheta_{2,rms} = 2.88$, and $\vartheta_{3,rms} = 0.96$. EOF-1 accounts for the bulk of the seasonal variability taking place close to the surface, and this explains the large rms value of the corresponding amplitude, whereas higher-order EOFs extend to increasingly deeper layers. The first three EOFs explain 99.6% of the total variance.

The behavior of peak-arrival times with respect to ϑ_1 variations, i.e., seasonal variations, is illustrated in Fig. 5. The KRAKEN[27] normal-mode code was used to calculate arrival patterns for each ϑ_1 value; the emitted signal was approximated by a Gaussian pulse. Only the peaks that can be continuously traced over the ϑ_1-variability range are plotted

in Fig. 5. A nonlinear character is evident for all sections and peaks; in particular, transition intervals can be seen, different for different peaks, where the nonlinearity is stronger. These intervals correspond to the passage from surface-reflected to refracted propagation, which, in terms of rays, occurs when the sound speed at the surface equals the sound speed at the ray up-turning depth. The latter is larger for deep rays—corresponding to early arrivals—than for shallower rays—corresponding to late arrivals. Accordingly, the transition will take place at larger ϑ_1 values for early arrivals than for late ones; this behavior is seen in Fig. 5. It is remarkable that the cutoff peak-arrival time along the southmost section W3–W4, Fig. 5(d), is nearly insensitive to ϑ_1 variations; in that case the source and receiver both lie on the channel axis (150 m). Neither the presence of the channel nor the sound speed at the channel axis is affected by the first EOF, since the latter extends up to 100 m only. The particular cutoff
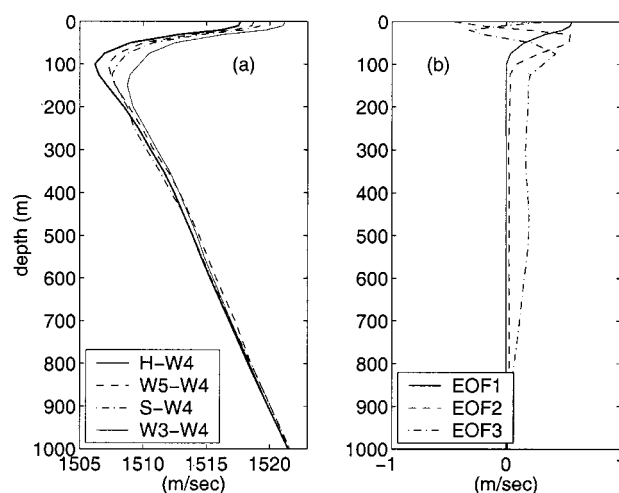

FIG. 4. (a) The basic reference sound-speed profiles along the four sections in the upper 1000 m. (b) The first three empirical orthogonal functions (EOFs) for the western Mediterranean basin.

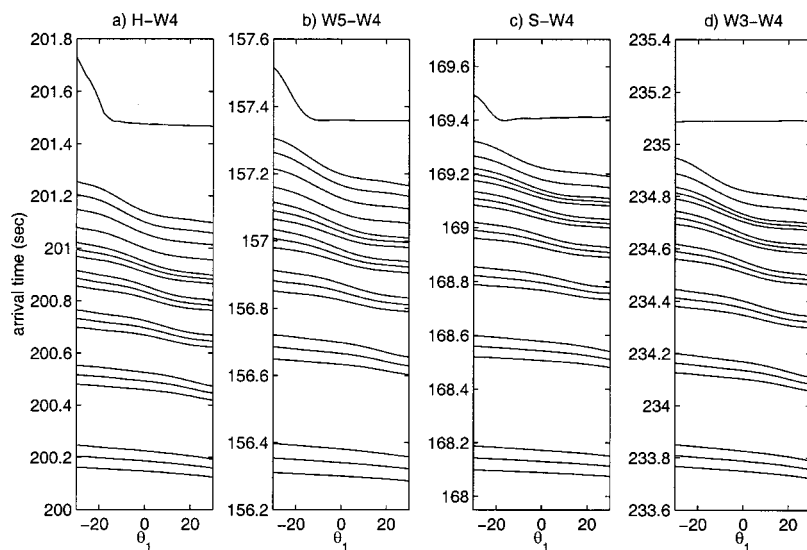E. K. Skarsoulis: Multi-section matched-peak inversion

FIG. 5. The predicted arrival times along the four sections as functions of the first EOF amplitude.

peak is affected by the higher-order EOFs only.

Using the model peaks shown in Fig. 5 the matched-peak inversion approach is applied to the data of Fig. 3 to perform offset calibration and inversion along the four sections, as well as navigation of the central mooring W4. For the calculation of the observation (influence) matrix the peak-arrival approach is used. To account for large-scale range-dependence effects, travel-time corrections are calculated from hydrographic data and applied to the cutoff peaks;[9] a cold bias is predicted along all sections, with an estimated mean delay of 53, 46, 25, and 6 ms along W3–W4, W5–W4, H–W4, and S–W4, respectively. The search space for the EOF-1 amplitude along each section is set to ± 8 about the historical value for each day of the year, whereas for the remaining EOFs it is set to ± 2.5 times the corresponding rms value. The discretization steps taken are $\delta \vartheta_1 = 0.7$, $\delta \vartheta_2 = 0.5$, and $\delta \vartheta_3 = 0.25$. The resulting discretization errors range from about 2 ms for the early arrivals to 10 ms or higher for the late ones, depending on the background state. A 10-ms observation/modeling error is considered for all peaks except the cutoff, for which a larger value of 50 ms is used to account for increased variability.[9,10]

The maximum horizontal deviations of the Thetis-2 transceivers are of the order of 50–100 m.[26] In this connection, the small-motion assumption is made for the horizontal displacements of the instrument W4. The navigation results for W4 support this assumption.

B. Results

Figure 6 shows the total number of identifications $\mathcal{M}$, over all sections and all transmissions, as a function of the time offset along S–W4 and H–W4; the time offsets for the W3–W4 and W5–W4 data have been arbitrarily set to zero, in accordance with the conclusion of Sec. III A. The global matching index $\mathcal{M}$ reaches its maximum value at a single point, denoted by an asterisk in Fig. 6, with $\Delta T_{S-W4} = 20$ ms and $\Delta T_{H-W4} = 0$, corresponding to 15 077 identified peaks over all sections and transmissions (an average of

about 17 identifications per section and transmission). The contours shown in Fig. 6 are separated by 10, starting from the maximum value.

It is seen from this figure that the time offsets close to the optimum, with respect to the total number of identified peaks, are distributed about a straight line with positive inclination passing through the optimum point (0,0.02). This means that an increase/decrease in the offset along H–W4 must be accompanied by an appropriate increase/decrease in the offset along S–W4 to ensure the best possible identification results, i.e., the best possible matching. This can be explained by looking at the geometry of the four sections in Fig. 2: since the offset along the nearly coaxial sections W3–W4 and W5–W4 is fixed to zero, there is only one degree of freedom left for the motion of W4, namely perpendicular to these sections, i.e., along a direction close to the east–west axis. This means that the resulting optimum offsets along H–W4 and S–W4 must be close to each other; this is observed in Fig. 6. Thus, the possibility to arbitrarily select any two of the time delays and the above behavior
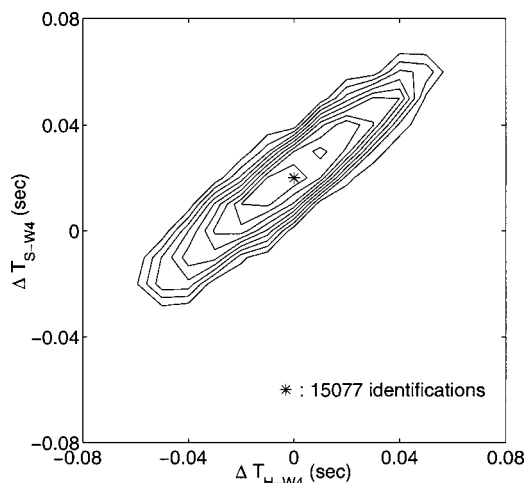

FIG. 6. Offset calibration: The global matching index $\mathcal{M}$ as function of the time offsets along H–W4 and S–W4, assuming zero offsets along W3–W4 and W5–W4. The maximum of $\mathcal{M}$ is denoted by an asterisk. The contours shown are separated by 10.
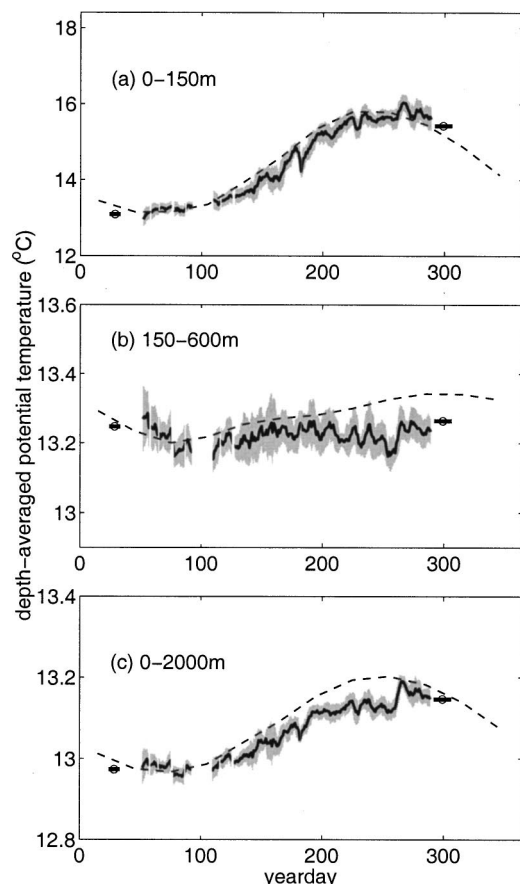
FIG. 7. Inversion results along H–W4: Evolution of depth-averaged potential temperatures in the 0–150, 150–600, and 0–2000-m layers. The retrieved mean temperatures (solid lines) and inversion errors (gray areas) are superimposed on the historical mean temperatures (dashed lines). Available hydrographic data are denoted through circles, with horizontal lines indicating the duration of observations.

FIG. 8. Inversion results along W5–W4 (description as in Fig. 7).

render the offset calibration practically one-dimensional.

The inversion results corresponding to the optimum time offsets along the four sections are shown in Figs. 7–10, in the form of depth-averaged temperatures over three layers: a surface layer, from the surface down to 150 m, an intermediate layer from 150 to 600 m, and a deep layer from the surface down to 2000 m, representing the total heat content of the water column. For converting the estimated sound speed to temperature a depth-dependent conversion relation has been used, of the form $\theta(z) = \theta_*(z) + d_*(z)[c(z) - c_*(z)]$ where θ_*, d_*, and c_* are depth functions estimated from historical data in the area of the experiment;[9] conversion errors have also been estimated and accounted for. The inversion results (mean values and rms errors) are shown through the solid lines and the gray areas, respectively, in Figs. 7–10. These results are based on simultaneous four-section inversions. In this connection, they cover only periods where simultaneous acoustic data exist along all four sections; e.g., the 15-day gap about yearday 100 in the W3–W4 data reflects in the inversion results along all sections.

The dashed lines in Figs. 7–10 represent the historical mean temperatures for each day of the year. Finally, the hydrographic data, collected before the start and after the end of the experiment, are marked through circles with horizontal
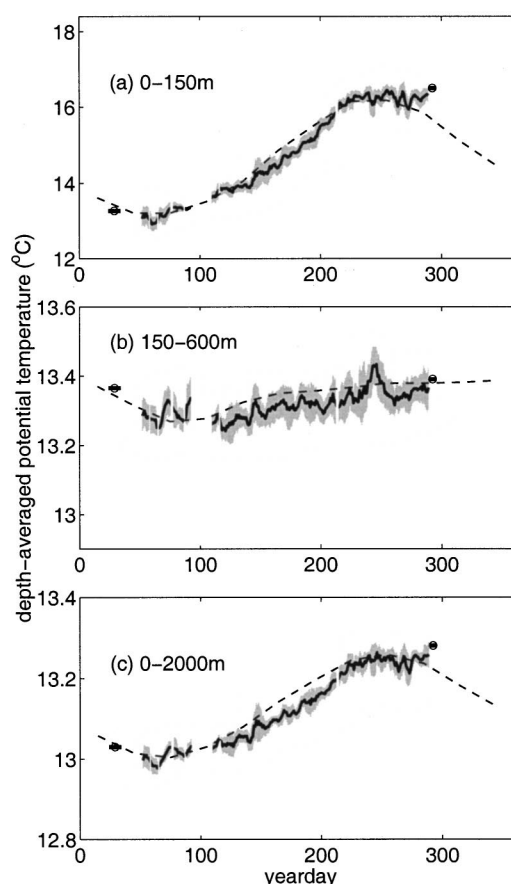
lines representing the duration of observations. In comparing these observations with the inversion results, their temporal distance (more than 30 days in some cases) as well as the temporal spread of the hydrographic data (reaching, e.g., 14 days in the case of late H–W4 data) have to be taken into account. The inversion results are in general agreement with the hydrographic data. Since the offset calibration in Fig. 6 has been based on the matched-peak approach, *not* on the hydrographic data, the inversion results and the hydrographic data are fully independent. The inversion results follow the anticipated gross seasonal behavior in the near-surface and the deep layer. The variability in the intermediate layer, below 150 m, is mainly due to mesoscale activity. A comparison of both the inversion results and the hydrographic data with the climatological data shows that there are significant deviations from the historical mean conditions in all three layers.

The horizontal displacement of the source W4 estimated from the multi-section matched-peak approach is shown in Fig. 11; for the time-to-distance conversion a reference sound speed $c_r = 1500$ m/s was used. The upper two panels of Fig. 11 show the north–south and east–west mean deviation along with the corresponding rms errors as a function of yearday. It is seen that the retrieved displacements exhibit a certain degree of temporal coherence, i.e., subsequent estimates of the displacement of W4 are statistically dependent on each other. This is particularly important considering the fact that subsequent receptions have been analyzed independently of each other.
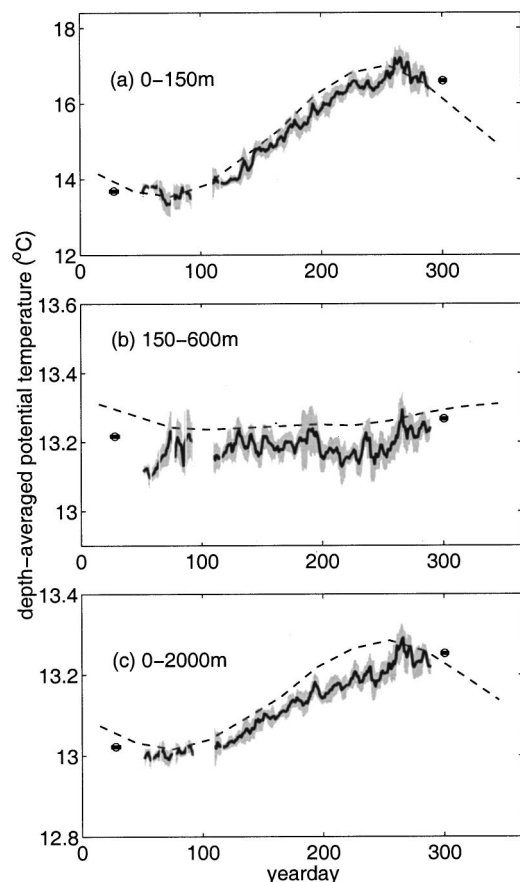
E. K. Skarsoulis: Multi-section matched-peak inversion

FIG. 9. Inversion results along S–W4 (description as in Fig. 7).

FIG. 10. Inversion results along W3–W4 (description as in Fig. 7).

The results shown are based on daily averages and accordingly, existing mooring motions with time scales less than 24 h are not resolved; moreover, such ''fast'' mooring motions may cause a certain degradation of the averaged data since their effects cannot be removed prior to averaging. Nevertheless, despite these shortcomings, the estimated horizontal deviations of the transceiver W4 explain most of the abrupt changes in the behavior of the observed travel-time data in Fig. 3. For example, the southward drift of the transceiver W4 between yeardays 170 and 175 [Fig. 11(a)] is seen in the observed travel times along the sections W5–W4 and W3–W4, close to the north–south axis. The arrivals along W5–W4 are delayed, whereas the ones along W3–W4 are advanced. Similarly, the drift of W4 to the south/southwest observed in Figs. 11(a) and (b) over the yeardays 50–75 causes a warm-bias effect (advancement of arrival times) along S–W4 and at the same time a delay (cold bias) in the arrival times along W5–W4, which can be seen in Fig. 3.

The lower panel in Fig. 11 shows the estimated horizontal trajectory of W4. The overall mean position of the transceiver is denoted by a dot. It is seen that the estimated horizontal deviations from the nominal position are less than 100 m, and in most cases less than 50 m. These values lie within the expectation limits for the particular mooring, and they further justify the small-motion assumption. The deviation of the overall mean position from the nominal position is about 16 m. This difference can be eliminated by appropriately modifying the time offsets, according to Eq. (23), such that
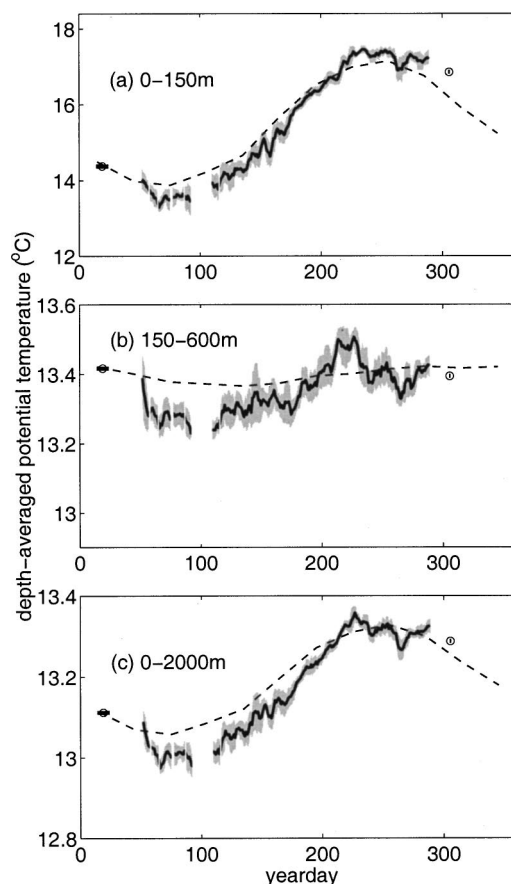
the nominal W4 position is shifted by 16 m to the north; see the concluding remarks of Sec. III A.

To assess the efficiency of the method for estimating the position of the central transceiver a synthetic test case is considered using simulated travel-time data: the measured arrival pattens along the four Thetis-2 sections are first corrected for the estimated displacements of W4, shown in Fig. 11, and then, assuming a harmonic motion of the central mooring, the travel-time data are modified accordingly. The synthetic data are used as input to the multi-section matched-peak approach. The navigation results for this synthetic case are shown in Fig. 12 along with the assumed harmonic motion (dashed line); the inversion results are nearly identical to those shown in Figs. 7–10 and are omitted. It is seen from Fig. 12 that the assumed mooring motion is reproduced with remarkable accuracy, with the dashed lines in most cases lying within the estimated error bars. This means that the method can separate the travel-time changes due to oceanographic conditions from those induced from motions of the central transceiver.

V. DISCUSSION—CONCLUSIONS

An extended matched-peak approach was presented allowing the simultaneous analysis of travel-time data from multiple tomographic sections, from a moving source or receiver to a number of peripheral fixed transceivers, to estimate the position of the moving instrument and the ocean state along the various sections. This can be useful, e.g., in
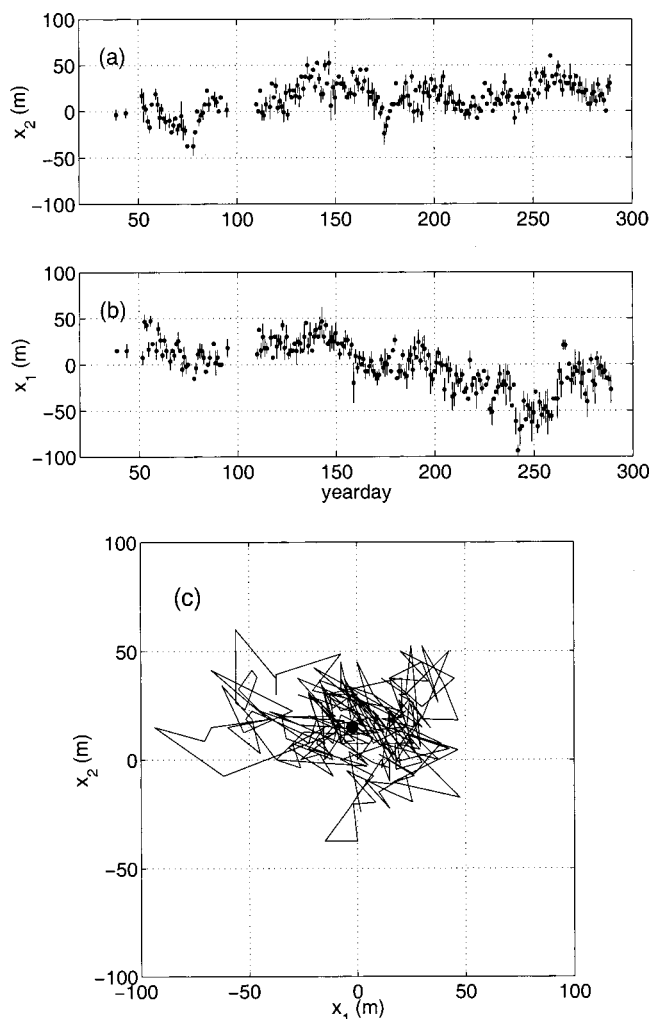
FIG. 11. Navigation results: The estimated (a) northward and (b) eastward displacements of the transceiver W4 and the corresponding rms errors. (c) The horizontal trajectory of the transceiver over the 9 months of the experiment. The overall mean position is denoted by a dot.
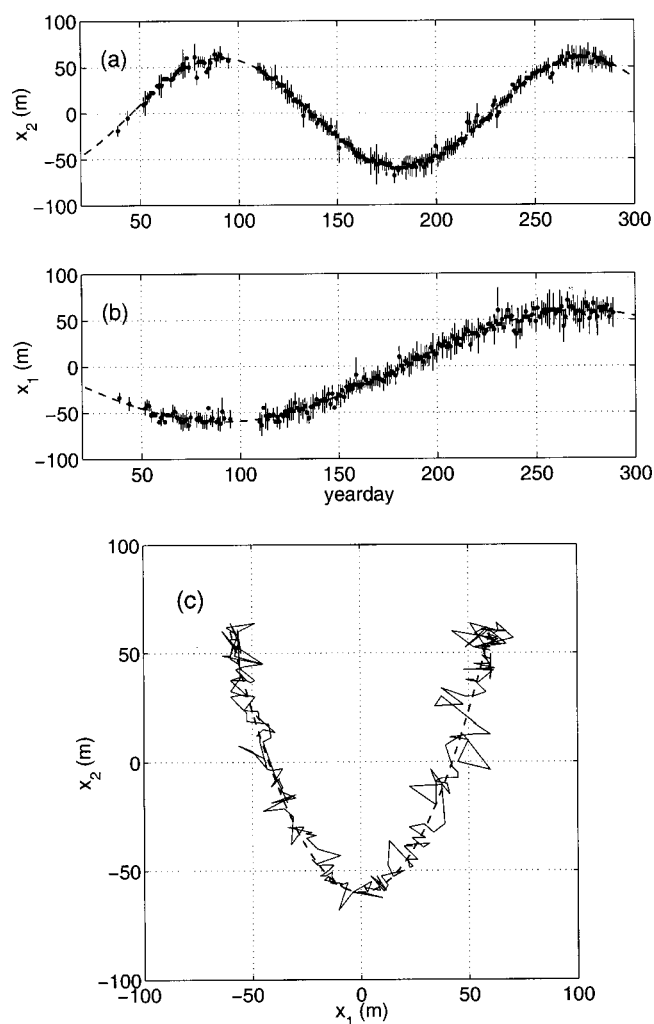
FIG. 12. Navigation results based on simulated travel-time data corresponding to a harmonic motion of the transceiver W4 (dashed lines). (a) Northward displacement; (b) eastward displacement. (c) The horizontal trajectory of W4.

case of missing navigation data for a particular transceiver within a tomographic array. The proposed scheme uses the simultaneous acoustic receptions along the sections originating/ending at the particular instrument to provide a solution to the inversion problem as well as an estimate for the instrument position. The solution consists of the kinematically compatible model states and instrument positions that maximize the joint matching index, i.e., the number of peak identifications over all sections.

A further problem addressed is the offset calibration along each section, which accounts for the difference between the actual and the nominal (best estimated) source–receiver range, as well as for internal instrument delays. This problem is usually solved by comparing measured acoustic arrival patterns and acoustic predictions based on hydrographic measurements, provided that the latter have been conducted simultaneously with the acoustic measurements along each section. The solution proposed here is based on a global matched-peak approach; the time offsets are estimated such that the total number of identifications over all sections and acoustic transmissions (global matching index) is maximized. This calibration approach is based on acoustic data

only, i.e., it does not require additional hydrographic measurements. In the case of small motions, the global matching index and the associated model states are invariant to translations of the (x_1, x_2)-coordinate system, corresponding to shifts of the nominal transceiver position. As a result, any two of the time offsets can be arbitrarily specified, reducing the dimension of the calibration problem by 2.

A main feature of the matched-peak approach is that it provides inversion and navigation results directly from travel-time data without requiring that identified peak tracks exist, thus enabling the automatic analysis of travel-time data, even in the presence of long interruption intervals between transmissions. Furthermore, by using an appropriate set of background states the problem of nonlinear model relations can be treated. All model states, i.e., all points within the parameter domain, are considered equally probable for describing a particular reception. The *a priori* rms values of the sound-speed parameters (e.g., the EOF amplitudes) are used to specify the extent of the parameter domain. The observation/modeling travel-time errors, together with the discretization errors, specify the maximum allowable tolerance for associating predicted and observed arrival times.

The inversion and position estimation errors depend on the travel-time data, i.e., they are in general different from transmission to transmission, in contrast to linear-inversion errors which are fixed and known *a priori*.

The application to the Thetis-2 data used the acoustic recordings of a moored source, for which navigation data were missing, at four other instruments, for which navigation data exist such that the effect of their horizontal motion could be removed from the acoustic data. The simultaneous acoustic measurements along the four sections were used to specify the optimum time offsets by applying the global matched-peak approach. Then, simultaneous four-section inversions were performed to specify the corresponding model states and source positions. The inversion results are in good agreement with the independent hydrographic observations. The time series of the estimated horizontal displacements of the central transceiver exhibit temporal coherence, i.e., subsequent estimates are statistically dependent on each other. The efficiency of the proposed approach for solving the navigation problem was illustrated using simulated data.

The above inversions covered only the cases of simultaneous data along all four sections, i.e., no results were produced in periods of data interruption along any of the sections. The best strategy in case of gaps in the data would be to adapt the analysis to the data available on each day. If data along a single section are available, then simple relative-time inversions can be performed. If there exist simultaneous data along two conodal sections (i.e., with a common mooring), the matched-peak approach can be used both for solving the inversion problem and for specifying the transceiver position. If the number of conodal sections is larger than two the same applies, but in addition the offset calibration problem can be addressed since only two time delays can be set arbitrarily, as shown in Sec. III A. The latter applies also to the case of two coaxial sections, with three moorings in line, since Eq. (13) becomes essentially one-dimensional (which means that only one time delay can be set arbitrarily).

The proposed multi-section matched-peak approach for solving the inversion and mooring navigation problem is based on the assumption that the horizontal deviation of the central transceiver is much smaller than the horizontal ranges of the corresponding sections. By relaxing this assumption the proposed method could be extended to address, e.g., the case of a central drifting source with moored/fixed peripheral receivers. Such a configuration might be useful, e.g., under ice, where the deployment of moored instruments is difficult.

ACKNOWLEDGMENTS

[1] W. H. Munk and C. Wunsch, "Ocean acoustic tomography: A scheme for large scale monitoring," Deep-Sea Res., Part A **26**, 123–161 (1979).

[2] W. H. Munk, P. F. Worcester, and C. Wunsch, *Ocean Acoustic Tomography* (Cambridge University Press, New York, 1995).

[3] J. L. Spiesberger, R. C. Spindel, and K. Metzger, "Stability and identification of ocean acoustic multipaths," J. Acoust. Soc. Am. **67**, 2011–2017 (1980).

[4] G. R. Legters, N. L. Weinberg, and J. G. Clark, "Long-range Atlantic acoustic multipath identification," J. Acoust. Soc. Am. **73**, 1571–1580 (1983).

[5] P. F. Worcester, "An example of ocean acoustic multipath identification at long range using both travel time and arrival angle," J. Acoust. Soc. Am. **70**, 1743–1747 (1981).

[6] B. M. Howe, P. F. Worcester, and R. C. Spindel, "Ocean acoustic tomography: Mesoscale velocity," J. Geophys. Res. **92**, 3785–3805 (1987).

[7] F. R. Martin-Lauzer and D. Mauuary, "Probabilistic ray identification: A new tool for ocean acoustic tomography," in P*roc. ICASSP 94* (Adelaide, 1994).

[8] E. K. Skarsoulis, G. A. Athanassoulis, and U. Send, "Ocean acoustic tomography based on peak arrivals," J. Acoust. Soc. Am. **100**, 797–813 (1996).

[9] E. K. Skarsoulis and U. Send, "One-step analysis of non-linear traveltime data in ocean acoustic tomography," J. Atmos. Ocean. Technol. **17**, 240–254 (2000).

[10] E. K. Skarsoulis, "A matched-peak inversion approach for ocean acoustic travel-time tomography," J. Acoust. Soc. Am. **107**, 1324–1332 (2000).

[11] U. Send, G. Krahmann, D. Mauuary, Y. Desaubies, F. Gaillard, T. Terre, J. Papadakis, M. Taroudakis, E. Skarsoulis, and C. Millot, "Acoustic observations of heat content across the Mediterranean Sea," Nature (London) **385**, 615–617 (1997).

[12] J. Marshall, F. Dobson, K. Moore, P. Rhines, M. Visbeck, E. d'Asaro, K. Bumke, S. Chang, R. Davis, K. Fisher, R. Garwood, P. Guest, R. Harcourt, C. Herbaut, T. Holt, J. Lazier, S. Legg, J. McWilliams, R. Pickart, M. Prater, I. Renfrew, F. Schott, U. Send, and W. Smethie, "The Labrador Sea deep convection experiment," Bull. Am. Meteorol. Soc. **79**, 2033–2058 (1998).

[13] B. Cornuelle, "Simulation of acoustic tomography array performance with untracked or drifting sources and receivers," J. Geophys. Res. **90**, 9079–9088 (1985).

[14] F. Gaillard, "Ocean acoustic tomography with moving sources or receivers," J. Geophys. Res. **90**, 11891–11898 (1985).

[15] W. H. Munk and C. Wunsch, "Up-down resolution in ocean acoustic tomography: Rays and modes," Deep-Sea Res., Part A **29**, 1415–1436 (1982).

[16] G. A. Athanassoulis and E. K. Skarsoulis, "Arrival-time perturbations of broadband tomographic signals due to sound-speed disturbances. A wave-theoretic approach," J. Acoust. Soc. Am. **97**, 3575–3588 (1995).

[17] J. L. Spiesberger and P. F. Worcester, "Perturbations in travel time and ray geometry due to mesoscale disturbances: A comparison of exact and approximate calculations," J. Acoust. Soc. Am. **74**, 219–225 (1983).

[18] W. H. Munk and C. Wunsch, "Ocean acoustic tomography: Rays and modes," Rev. Geophys. Space Phys. **21**, 777–793 (1983).

[19] E. C. Shang, "Ocean acoustic tomography based on adiabatic mode theory," J. Acoust. Soc. Am. **85**, 1531–1537 (1989).

[20] R. W. Preisendorfer and C. D. Mobley, *Principal Component Analysis in Meteorology and Oceanography* (Elsevier, Amsterdam, 1988).

[21] E. C. Shang and Y. Y. Wang, "On the calculation of modal travel time perturbation," Sov. Phys. Acoust. **37**, 411–413 (1991).

[22] For example, if a 3-km mooring leans to the side by 100 m the time shift associated with the horizontal displacement of the mooring top (100 m) is about 65 ms. The time shift due to the vertical displacement of the mooring top will be 0.5 ms at most, assuming that the mooring remains linear.

[23] L. Brekhovskikh and O. Godin, *Acoustics of Layered Media II. Point Sources and Bounded Beams* (Springer, Berlin, 1992).

[24] F. B. Jensen, W. A. Kuperman, M. B. Porter, and H. Schmidt, *Computational Ocean Acoustics* (AIP, New York, 1994).

[25] Thetis-2, A pilot tomography system for monitoring the western Mediterranean basin, Final Report, edited by U. Send, EU MAST-2 project CT91-0006, March 1996.

[26] Thetis group, A pilot tomography system for monitoring the western Mediterranean basin, Tomography Data Report, EU MAST-2 project CT91-0006, March 1996.

[27] M. B. Porter and E. L. Reiss, "A numerical method for ocean acoustic normal modes," J. Acoust. Soc. Am. **76**, 244–252 (1984).